Journal of Materials Chemistry A

Accepted Manuscript

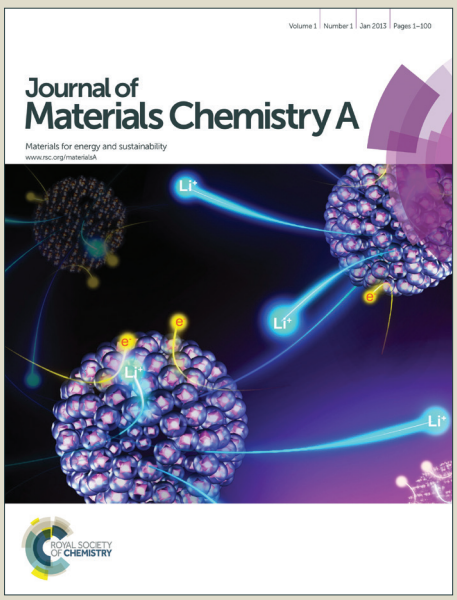

ROYAL SOCIETY OF CHEMISTRY

www.rsc.org/materialsA

Mushroom-like Au/$NiCo_2O_4$ nanohybrid as high-performance binder-free catalytic cathode for lithium–oxygen batteries

Fangfang Tu,[a] Jian Xie,[*ab] Shichao Zhang,[c] Gaoshao Cao,[b] Tiejun Zhu[a] and Xinbing Zhao[ab]

[a]*State Key Laboratory of Silicon Materials, School of Materials Science and Engineering, Zhejiang University, Hangzhou 310027, China. E-mail: xiejian1977@zju.edu.cn; Fax: +86-571-87951451; Tel: +86-571-87952181*

[b]*Key Laboratory of Advanced Materials and Applications for Batteries of Zhejiang Province, Hangzhou 310027, China*

[c]*School of Materials Science and Engineering, Beijing University of Aeronautics and Astronautics, Beijing 100191, China*

† Electronic supplementary information (ESI) available: SEM and Raman of 3D-G, nitrogen adsorption and desorption isotherms of Au/$NiCo_2O_4$/3D-G and $NiCo_2O_4$/3D-G, SEM images of $NiCo_2O_4$/3D-G after immersion in different solutions, SEM image of Au/$NiCo_2O_4$/3D-G and (b) the corresponding EDS mapping in a wide range, Nyquist plots of Li–O_2 batteries with different catalytic cathodes, the electrochemical performance of Li–O_2 batteries with 3D-G and Au/3D-G catalysts, TEM and SAED of the Au/$NiCo_2O_4$/3D-G electrode, Nyquist plots of Li–O_2 battery with Au/$NiCo_2O_4$/3D-G catalyst at different states, SEM of $NiCo_2O_4$/3D-G electrode after discharge and recharge on the 10^{th} cycle, and SEM images and Li1s XPS of Au/$NiCo_2O_4$/3D-G electrodes at different states . See DOI:

Abstract

$Li–O_2$ (or Li–air) battery currently represents a hot topic in the field of energy storage and conversion. The electrochemical performance of $Li–O_2$ battery depends largely on the material and architecture of the catalytic cathode. In this work, we propose a unique design of binder-free catalytic cathode for $Li–O_2$ batteries. The electrode consists of novel mushroom-like $Au/NiCo_2O_4$ nanohybrid on three-dimensional graphene (3D-G) grown directly on the skeleton of Ni foam. The $Au/NiCo_2O_4$/3D-G catalyst exhibits good catalytic effect for $Li–O_2$ batteries, where Au directs the growth of Li_2O_2 mainly on the top of mushroom-like $Au/NiCo_2O_4$, and induces the crystallization of Li_2O_2 into thin-flake or thin-film form that is found to decompose relatively easily compared with large-particle form upon charge. Mushroom-like $NiCo_2O_4$ provides additional catalytic sites and acts as the support for both Au and Li_2O_2. $Li–O_2$ battery with $Au/NiCo_2O_4$/3D-G catalyst can deliver a capacity of around 1275 mAh g^{-1} at 42.5 mA g^{-1}. When the capacity is limited at 510 mAh g^{-1}, the $Li–O_2$ battery can sustain a stable cycling for 40 times.

Introduction

Although Li-ion batteries recently show promising applications in electric vehicles (EVs) and hybrid electric vehicles (HEVs), the energy density of current Li-ion batteries is far from satisfying the requirements of EVs and HEVs.[1] Since first reported by Abraham et al.,[2] Li–O_2 (or Li–air) batteries have attracted a great attention due to their extremely high theoretical energy density of 11680 Wh kg^{-1} (3548 Wh kg^{-1} including oxygen), which is nearly equal to that of gasoline (13000 Wh kg^{-1}).[3–5] However, Li–O_2 batteries still face significant challenges before practical applications,[4,6–8] including sluggish oxygen reduction/evolution reaction (ORR/OER) kinetics related to the formation of insulating Li_2O_2,[9,10] and the accumulation of the byproducts (e.g. Li_2CO_3) due to the side reactions of Li_2O_2 (or its intermediate LiO_2) with electrolyte or carbon.[11,12] Typical binder, for example, polyvinylidene fluoride (PVDF), is also unstable in contact with Li_2O_2 (or LiO_2) with the formation LiF and –(CH=CF)– like species.[13] A combination of these detrimental factors results in large overpotential, poor rate capability and limited cycle life of Li–O_2 batteries.

The use of catalysts has proven to be an effective measure to improve ORR/OER kinetics.[14,15] Although non-precious catalysts,[16] such as carbon materials[17,18] and transition metals oxides (TMOs: MnO_2,[19,20] Co_3O_4,[21] $NiCo_2O_4$,[22] etc), are preferred for practical applications, they exhibit limited catalytic activity. In contrast, noble metals, Au,[23] Pt,[24] PtAu,[25] Pd,[26] etc., show high catalytic activity towards ORR/OER. For instance, Peng et al.[23] has reported that Li–O_2 battery with gold porous electrode could show a low overpotential and sustain a stable cycling up to 100 times. Lim et al.[24] has found that Pt nanoparticles on carbon nanotubes could direct the growth of Li_2O_2, leading to reduced overpotential. Considering the high cost of noble metals, a compromise can be made by loading noble metals on a matrix, for example TMOs.[27] Compared with carbon materials, TMOs are more stable against the attack of Li_2O_2 (or LiO_2) and/or are more catalytically active towards ORR/OER.[28–30] Besides the use of catalysts, the architecture of air electrode is another concern since it involves the deposition of insulating/insoluble Li_2O_2 and the byproducts.

It is well known that the charge potential of Li–O_2 batteries is greatly influenced by the

morphology and distribution of discharge products. However, the exact effect of morphology of Li_2O_2 on its decomposition upon charge still remains controversial. Several groups have reported that large Li_2O_2 particles require high charge potential for their limited contact with catalysts, while thin Li_2O_2 deposits can decompose at low potentials due to their larger surface area, enhanced surface electronic conductivity and improved charge transfer at Li_2O_2/catalyst interfaces.[31,32] By contrast, Lu et al. indicates that large toroid-like Li_2O_2 can be charged at lower potential compared with film-like Li_2O_2 since the toroids are made up of nanosized grains and grain boundaries, which brings good electronic conductivity.[15] In this work, the effect of morphology of Li_2O_2 on its decomposition will be investigated by directing the Li_2O_2 growth with catalyst.

In this work, we propose a new design of air electrode by directly depositing Au-decorated $NiCo_2O_4$ (Au/$NiCo_2O_4$) onto the skeleton of three-dimensional graphene (3D-G) coated Ni foam. Nickel foam was considered as a good catalyst support due to its high porosity, stability and electrical conductivity.[33] Before the Au/$NiCo_2O_4$ deposition, graphene was first deposited on Ni foam to construct a 3D-G architecture. It has been reported that 3D macroporous graphene architecture can combine the superior intrinsic properties of graphene with additional 3D porous structure, which not only maintains high electrical conductivity and good chemical inertia of graphene, but also provides a high specific area and numerous porous channels to improve ion and electron transport.[34,35] $NiCo_2O_4$ was selected as the support for Au since it is highly efficient for ORR and OER.[22,36] We found that the top of $NiCo_2O_4$ nanowires could be converted into flower-like nanosheets with decorated Au nanoparticles after immersion in $HAuCl_4 \cdot 3H_2O$ aqueous solution, while the bottom of the nanowires was kept intact without Au decoration, leading to the formation of a mushroom-like structure as shown in Fig. 1. Importantly, the presence of Au could change the crystallization habit of Li_2O_2, alleviating the electrode passivation by directing the deposition of Li_2O_2 in a desirable form and at a favorable position of the electrode. The Au/$NiCo_2O_4$/3D-G catalyst demonstrates superior catalytic performance because of its unique structure and component.

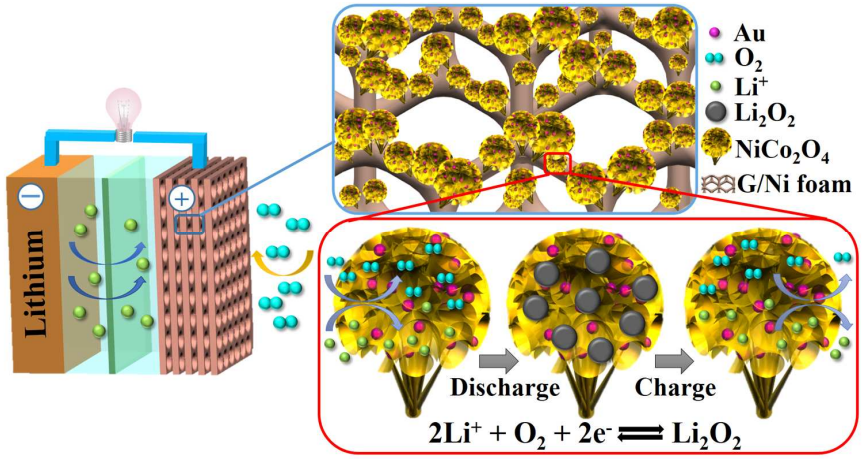

Fig. 1 Schematic presentation of the structure and working mechanism of Li–O_2 battery with Au/$NiCo_2O_4$/3D-G catalytic cathode.

Experimental section

Preparation of Ni foam supported three-dimensional graphene (3D-G)

Nickel foam (density: ~285 g m^{-2}, thickness: ~1.6 mm, porosity: ≥96%, Heze Tianyu Technology Development Co., Ltd, China) was used as the 3D scaffold template to grow 3D-G by chemical vapor deposition (CVD) method.[37] Ni foam was first cut into pieces of 5 cm×20 cm and placed into the quartz tube of a horizontal tube furnace, followed by heating to 1000 ^oC rapidly at 100 ^oC min^{-1} under Ar flow of 500 standard-state cubic centimeters per minute (sccm) and annealing at 1000 ^oC for 5 min to clean the surface of Ni foam. Afterwards, ethanol was introduced into the quartz tube by Ar flow at 250 sccm to initiate the graphene growth. After reaction at 1000 ^oC for 5 min, the furnace was cooled down to room temperature in Ar flow of 500 sccm. The graphene loading on Ni foam is 0.85 mg cm^{-2} after the reaction.

Preparation of Ni foam supported $NiCo_2O_4$/3D-G

In a typical synthesis, $Ni(NO_3)_2 \cdot 6H_2O$ (2 mmol), $Co(NO_3)_2 \cdot 6H_2O$ (4 mmol), and urea (24 mmol) were dissolved into deionized (DI) water (60 mL) under vigorous magnetic stirring. The clear pink solution was then transferred into a Teflon-lined stainless steel autoclave and a piece of Ni foam supported 3D-G (2.5×2.5 cm^2) was put into the autoclave. The autoclave was sealed and heated in

an electric oven at 120 °C for 6 h. After cooling down to room temperature, the hydrothermal product was taken out from the autoclave. Ni foam supported $NiCo_2O_4$/3D-G was obtained after washing the product with DI water and absolute ethanol repeatedly, drying under vacuum at 60 °C overnight, and annealing at 400 °C for 3 h in air. The loading of $NiCo_2O_4$ on 3D-G is 0.78 mg cm^{-2}.

Preparation of Ni foam supported Au/$NiCo_2O_4$/3D-G

$HAuCl_4 \cdot 3H_2O$ (16 mg) was added into DI water (15 mL) to form a homogeneous solution under magnetic stirring. Ni foam supported $NiCo_2O_4$/3D-G was immersed in the solution for 12 h. After the immersion, the product was washed with DI water and absolute ethanol repeatedly, and dried at 60 °C under vacuum overnight. The loading of Au on $NiCo_2O_4$/3D-G is 0.37 mg cm^{-2}. For comparison, Ni foam supported Au/3D-G was also prepared in a similar way without $NiCo_2O_4$ deposition.

Materials characterization

The X-ray diffraction (XRD) patterns were obtained on a Rigaku D/Max-2550pc powder diffractometer with Cu K_α radiation (λ = 1.541 Å). X-ray photoelectron spectra (XPS) were acquired on a KRATOS AXIS ULTRA-DLD spectrometer using a monochromatic Al K_α radiation ($h\nu$ = 1486.6 eV). The morphology of the samples was characterized by field-emission scanning electron microscope (SEM) on a FEI-sirion microscope, transmission electron microscopy (TEM), and high-resolution TEM (HRTEM) on a JEM 2100F microscope. Raman spectrum was measured by a Jobin-Yvon Labor Raman HR-800 system with a 514.5 nm Ar-ion laser. Nitrogen adsorption and desorption isotherms were measured on an AUTOSORB-1-C apparatus.

Electrochemical measurements

Swagelok-type cells were used to investigate the electrochemical performance of Li–O_2 batteries. Battery assembly was carried out in an Ar-filled glove box. The Li–O_2 batteries were composed of lithium foil as anode, glass fiber membrane (Whatman) as separator, Au/$NiCo_2O_4$/3D-G ($NiCo_2O_4$/3D-G, Au/3D-G or 3D-G) supported on Ni foam as cathode, and 1,2-dimethoxyethane

(DME) containing 0.1 M $LiClO_4$ as electrolyte. The batteries were purged with O_2 flow of 30 sccm for 10 min before testing. Galvanostatic cycling was performed on a Neware battery tester (Shenzhen, China) at 2.0–4.5 V or 2.2–4.3 V. Cyclic voltammetry (CV) scanning was conducted on a VersaSTAT3 electrochemistry workstation at 0.05 mV s^{-1} between 2.0 and 4.5 V. Electrochemical impedance spectroscopy (EIS) measurements were performed on the workstation by applying an AC signal of 5 mV amplitude over the frequency range 10^{-2}–10^5 Hz. All of the electrochemical measurements were carried out at room temperature.

Results and discussion

3D-G was prepared by a template-directed CVD method using 3D Ni foam as the template. $NiCo_2O_4$ was grown on 3D-G coated Ni foam by a hydrothermal method. Au decoration on $NiCo_2O_4$ was realized by a facile immersion process. Fig. 2a shows the XRD patterns of Au/$NiCo_2O_4$/3D-G and $NiCo_2O_4$/3D-G supported on Ni foam. XRD patterns clearly indicate the formation of phase-purity $NiCo_2O_4$ for both samples and the formation of Au in Au/$NiCo_2O_4$/3D-G sample. The chemical composition and oxidation state of Au/$NiCo_2O_4$/3D-G electrode were checked by XPS. The survey spectrum in Fig. 2b shows the expected elements in Au/$NiCo_2O_4$/3D-G. The Ni2p spectrum (Fig. 2c) can be fitted by two spin-orbit doublets (Ni^{2+} and Ni^{3+}) and two satellites (denoted as "Sat.").[38,39] Co2p spectrum (Fig. 2d) is also fitted by two spin-orbit doublets (Co^{2+} and Co^{3+}).[38,39] The O 1s spectrum (Fig. 2e) can be divided into three peaks for different forms of oxygen (O1, O2, and O3).[38–40] The O1 peak at 529.5 eV is related to typical metal-oxygen bonds, the O2 peak at 530.0 eV corresponds to oxygen in OH^- groups, and the O3 peak at 531.5 eV is related to oxygen ions in low oxygen coordination at the surface.[38–40] The Au 4f spectrum (Fig. 2f) exhibits two peaks located at 84.0 and 87.7 eV, which is typical of Au^0 oxidation state,[41] confirming the formation of metallic Au.

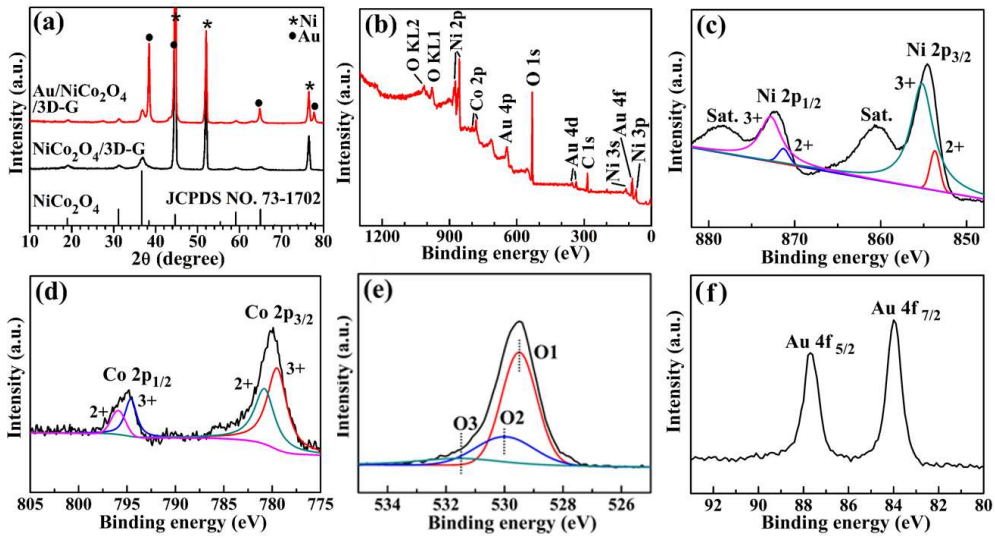

Fig. 2 (a) XRD patterns of $NiCo_2O_4$/3D-G and Au/$NiCo_2O_4$/3D-G on nickel foam, (b) XPS survey spectrum of Au/$NiCo_2O_4$/3D-G, and (c) Ni2p, (d) Co2p, (e) O1s and (f) Au4f XPS of Au/$NiCo_2O_4$/3D-G.

Fig. 3 presents the SEM images of $NiCo_2O_4$/3D-G and Au/$NiCo_2O_4$/3D-G on Ni foam. Low-magnification images in Fig. 3a,d indicate that both $NiCo_2O_4$/3D-G and Au/$NiCo_2O_4$/3D-G were deposited only on the skeleton of Ni foam, copying its interconnected 3D scaffold structure with its large pores intact. The 3D-G, the interlayer between $NiCo_2O_4$ and Ni foam, exhibits a few-layered nature as revealed by the wrinkles in SEM image (See Fig. S1b in the ESI†) and the strong 2D Raman peak (see Fig. S1c in the ESI†). For $NiCo_2O_4$/3D-G, slender $NiCo_2O_4$ nanowires with a sharp tip are uniformly arranged on 3D-G (Fig. 3b,c). Typical $NiCo_2O_4$ nanowires have a diameter around 60 nm and a length of several microns. After immersion in a $HAuCl_4 \cdot 3H_2O$ aqueous solution, the top of the nanowires has been converted into flower-like nanosheets with Au nanoparticles decorated on the surface (Fig. 3e,f). As a result, a mushroom-like structure has been constructed. This conversion is favorable since it can supply more catalytic sites, increase the contact with electrolyte, and facilitate the deposition of Li_2O_2 by increasing the surface area (see Fig. S2 in the ESI†).

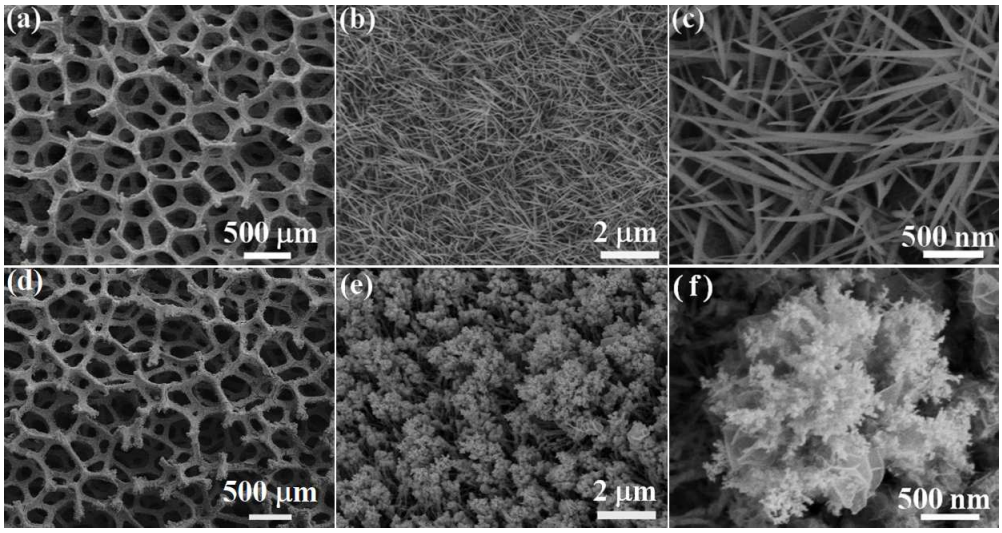

Fig. 3 SEM images of (a–c) $NiCo_2O_4$/3D-G and (d–f) Au/$NiCo_2O_4$/3D-G on nickel foam.

It is proposed that the formation of sheet-like $NiCo_2O_4$ is realized through a dissolution and recrystallization process catalyzed by Au. To clarify this assumption, we performed a series of experiments by immersing $NiCo_2O_4$/3D-G in various aqueous solutions containing HCl, H_2PtCl_6, Na_2PdCl_4, and Na_2PdCl_4/HCl under similar conditions. After immersion in H_2PtCl_6 solution, the conversion of nanowires into nanosheets could also occur (see Fig. S3b in the ESI†). In contrast, the nanowires structure of $NiCo_2O_4$ is still preserved in HCl (see Fig. S3a in the ESI†) or Na_2PdCl_4 solution (see Fig. S3c in the ESI†). Of note is that the conversion is also possible by immersing $NiCo_2O_4$ in a mixed solution containing Na_2PdCl_4 and HCl (see Fig. S3d in the ESI†). This indicates that the conversion could only occur via a combined effect of acidic condition and presence of noble metal.

TEM, HRTEM and energy dispersive X-ray spectrometry (EDS) mapping were applied to further investigate the microstructure of Au/$NiCo_2O_4$/3D-G. Fig. 4a shows a single mushroom-like structure composed of a nanowire and flower-like nanosheets with decorated nanoparticles. Fig. 4b,c presents the HRTEM images of two selected domains (1 and 2) in Fig. 4a. The fringe spacings of 0.23 and 0.20 nm in Fig. 4b correspond to the (111) and (200) planes of Au, and those of 0.24 and 0.47 nm in Fig. 4c correspond to the (311) and (111) planes of $NiCo_2O_4$. The dark-filed TEM image and the corresponding EDS mapping (Fig. 4d–h) further prove that the dark part on the

nanosheets is Au, and that no Au is present on the nanowires part of the mushroom-like $NiCo_2O_4$. The EDS mapping in a wider range was also given (see Fig. S4 in the ESI†), which indicates that Ni, Co, O and Au elements are dispersed evenly in the nanohybrid and reveals the uniformity of the obtained electrode.

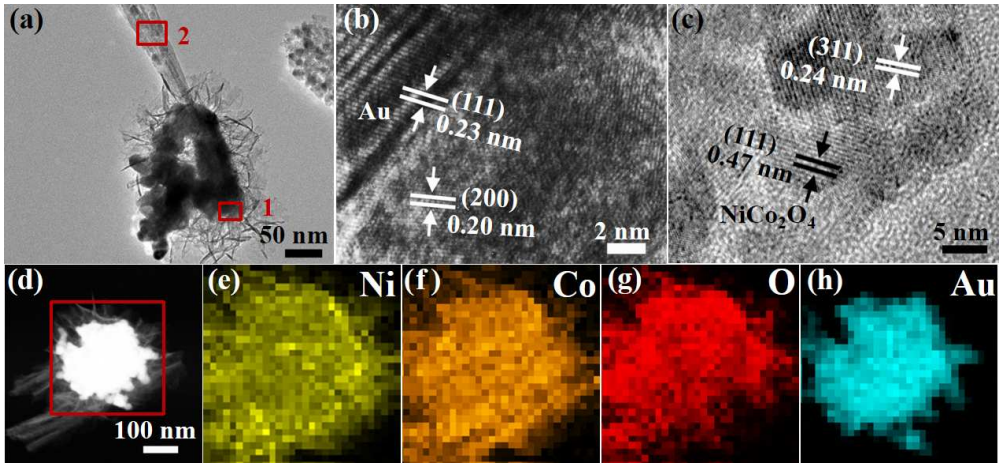

Fig. 4 TEM and EDS of the sample from the Au/$NiCo_2O_4$/3D-G electrode: (a) TEM image of a single mushroom-like structure, (b) HRTEM image of selected area 1 in (a), (c) HRTEM image of selected area 2 in (a), and (d–h) dark-field TEM image and the corresponding EDS mapping.

The electrocatalytic activity of Au/$NiCo_2O_4$/3D-G was evaluated in Li–O_2 batteries and compared with those of $NiCo_2O_4$/3D-G, Au/3D-G and 3D-G. All of the current densities and specific capacities of the electrodes are normalized by the total weight of the components on Ni foam. For example, the current density and specific capacity of the Au/$NiCo_2O_4$/3D-G electrode are normalized by the total weight of Au, $NiCo_2O_4$ and 3D-G on nickel foam. Fig. 5a shows the first discharge-charge curves of Li–O_2 batteries with Au/$NiCo_2O_4$/3D-G catalytic cathodes at 42.5 mA g^{-1} (0.086 mA cm^{-2}). The Li–O_2 battery with Au/$NiCo_2O_4$/3D-G catalytic cathodes can deliver a discharge capacity of 1275 mAh g^{-1} and a relatively low mid-capacity overpotential (defined as the overpotential at half capacity) of 1.01 V. Note that most of the discharge product can be decomposed below 4.0 V.

EIS is used to understand the different catalytic effects between these catalysts (see Fig. S5 in the ESI†). The Nyquist plots and the corresponding fitting (see Table S1 in the ESI†) clearly

indicate that the Au introduction considerably reduces R_e and R_{ct} of the $NiCo_2O_4$/3D-G electrode, which is closely related to the mushroom-like structure and the decoration of highly catalytic and conductive Au. CV scanning was performed to study the ORR and OER of Au/$NiCo_2O_4$/3D-G catalyst (Fig. 5b). Apart from the first cycle, the CV plots show one reduction peak at 2.35 V and three oxidation peaks at around 3.4, 3.7 and 4.0 V, respectively. Multiple oxidation peaks and successive charge plateaus suggest that the decomposition of Li_2O_2 undergoes a stepwise process. As previously reported,[42–45] Li_2O_2 is first partially de-lithiated to form $Li_{2-x}O_2$ species at low potentials, followed by the oxidation of bulk Li_2O_2 at high potentials. Another possible explanation for the two-stage (or multi-stage) de-lithiation is that thin Li_2O_2 deposits can decompose at low potentials through electron tunneling, while thick Li_2O_2 deposits decompose at high potentials through polaron hopping.[32] Fig. 5c presents the rate capability of the Au/$NiCo_2O_4$/3D-G catalyzed Li–O_2 battery with the capacity limited at 510 mAh g^{-1}. At 170 mA g^{-1} (0.344 mA cm^{-2}), the battery can show a low average charge potential at around 4.0 V and a high discharge potential at 2.65 V.

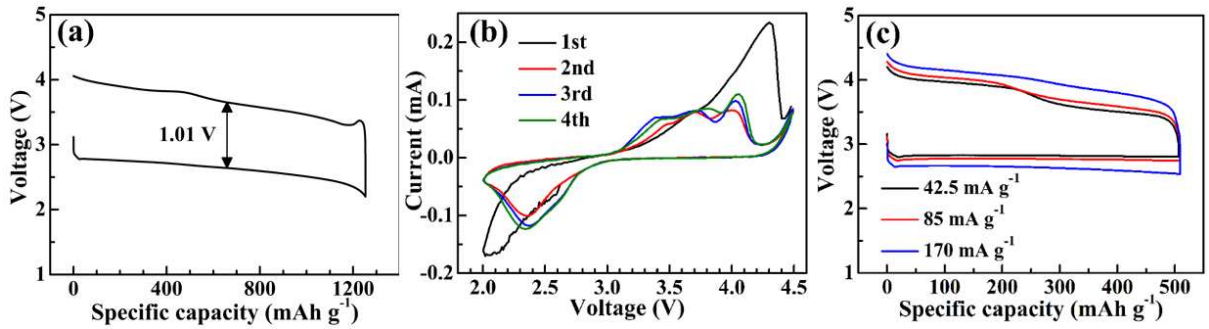

Fig. 5 (a) The 1st charge-discharge curves of Li–O_2 batteries with Au/$NiCo_2O_4$/3D-G and $NiCo_2O_4$/3D-G cathodes at 42.5 mA g^{-1}, and (b) CV plots at 0.05 mV s^{-1} and (c) rate performance at 510 mAh g^{-1} of Au/$NiCo_2O_4$/3D-G catalyzed Li–O_2 batteries.

The stability of catalytic activity of Au/$NiCo_2O_4$/3D-G and $NiCo_2O_4$/3D-G cathodes was evaluated by galvanostatic cycling the Li–O_2 batteries under 42.5 mA g^{-1} at 2.0–4.5 V with the capacity limited at 510 mAh g^{-1}. As seen in Fig. 6a, the discharge plateau of Au/$NiCo_2O_4$/3D-G

catalyzed battery is 2.80 V in the first cycle, and is stabilized at around 2.60 V up to 40 cycles. The charge curves exhibit two obvious plateaus at 3.45 and 3.95 V, indicating the stepwise decomposition feature of Li_2O_2. By contrast, this phenomenon can hardly be seen for the $NiCo_2O_4$/3D-G catalyzed battery (Fig. 6d). Fig. 6a also demonstrates that most of the Li_2O_2 can be decomposed below 4.0 V during 40 cycles. This is favorable since high charge potential will unavoidably lead to undesirable side reactions, for instance electrolyte decomposition. Fig. 6b illustrates the enlarged view of the rectangular area in Fig. 6a, which clearly shows that the charge potential is on the decrease till the 30^{th} cycle, indicative of the activation process of the catalytic effect of Au. For the $NiCo_2O_4$/3D-G catalyzed battery, however, this process is not obvious (Fig. 6e).

As shown in Fig. 6c, the Li–O_2 battery with Au/$NiCo_2O_4$/3D-G catalytic cathode can sustain a stable cycling for 40 times. After that, the battery performance begins to degrade and finally fails. For the battery using $NiCo_2O_4$/3D-G catalyst, the stable cycling can last only 8 cycles (Fig. 6f). Obviously, Li–O_2 battery with Au/$NiCo_2O_4$/3D-G catalyst demonstrates significantly improved electrochemical performance than that with $NiCo_2O_4$/3D-G catalyst. For comparison, the electrochemical properties of Li-O_2 batteries with Au/3D-G and 3D-G catalysts were also evaluated under same conditions, namely, at a current density of 42.5 mA g^{-1} with the specific capacity limited at 510 mAh g^{-1}. As seen in Fig. S6 in the ESI†, in both cases, the battery cannot sustain a capacity of 510 mAh g^{-1} and rapid capacity fade is evident. In addition, both batteries demonstrate obviously higher overpotentials than the Au/$NiCo_2O_4$/3D-G catalyzed one.

It suggests that the performance enhancement can be ascribed to the unique microstructure and component of the Au/$NiCo_2O_4$/3D-G catalytic cathode. In this cathode, Au plays an important role in ensuring the good catalytic activity of the Au/$NiCo_2O_4$/3D-G cathode. First, Au increases the electrode conductivity of $NiCo_2O_4$/3D-G (see Fig. S5 in the ESI†) as mentioned above; second, Au provides highly efficient catalytic centers for ORR/OER; third, Au changes the crystallization behavior of Li_2O_2 in a favorable way which will be discussed below. Besides Au, the

mushroom-like $NiCo_2O_4$ is also responsible for the high catalytic performance of the Au/$NiCo_2O_4$/3D-G electrode. The mushroom-like $NiCo_2O_4$ has multiple functions in the cathode: (1) $NiCo_2O_4$ also shows good catalytic activity evidenced from the reduced overpotential of $NiCo_2O_4$/3D-G catalyzed Li–O_2 battery (Fig. 6d) compared with 3D-G catalyzed one (see Fig. S6a in the ESI†); (2) $NiCo_2O_4$ acts as the support for Au nanoparticles; (3) $NiCo_2O_4$ with sheet-like top is also a good support for Li_2O_2 deposition due to the large surface area, while the wire-like bottom is left almost intact for oxygen and Li-ion diffusion.

It should be noted that the decomposition of Li_2O_2 may become kinetically sluggish if it is deposited on Au/$NiCo_2O_4$ instead of conductive 3D-G. However, in situ SEM observation of the formation and decomposition of Li_2O_2 on carbon nanotube (CNT) showed that the decomposition of Li_2O_2 can occur on the surface of Li_2O_2 instead of on the Li_2O_2–CNT interface or on the Li_2O_2–electrolyte interface.[46] It means that the electronic conductivity of Li_2O_2 itself can support its decomposition, and that the mass transfer (O_2 release and diffusion) may be of equal importance as the charge transfer for Li_2O_2 decomposition. In the Au/$NiCo_2O_4$/3D-G electrode, Au/$NiCo_2O_4$ may provide acceptable conductive channels for charge transfer reaction, while its unique structure facilitates the rapid mass transfer such as O_2 release and diffusion. This is can explain lower charge overpotential of Au/$NiCo_2O_4$/3D-G (Fig. 6a) compared with Au/3D-G (see Fig. S6c in the ESI†).

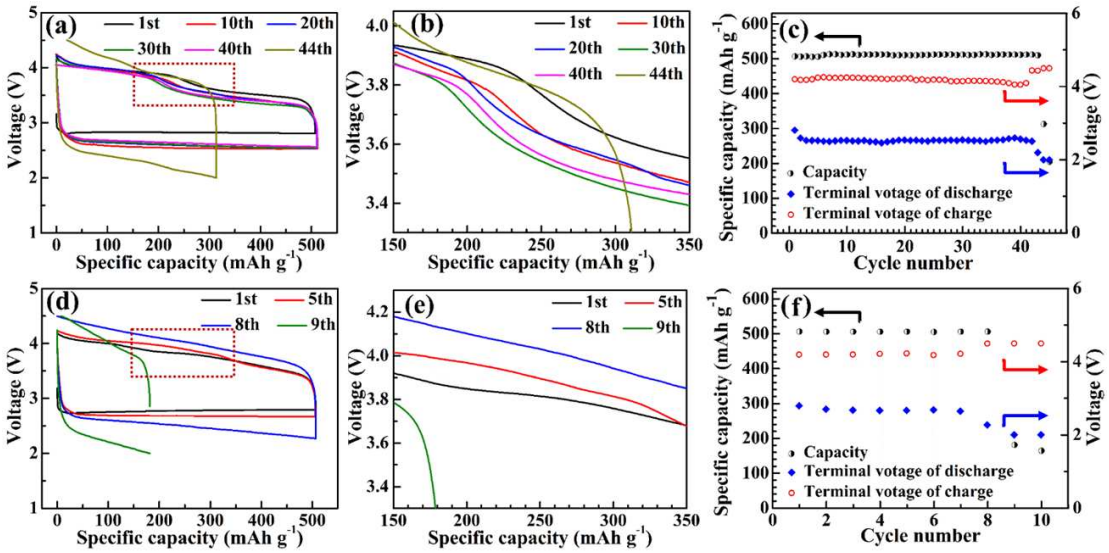

Fig. 6 (a–c) Voltage profiles and cycling performance of Li–O_2 battery with Au/$NiCo_2O_4$/3D-G electrode under 42.5 mA g^{-1} at a limited capacity of 510 mAh g^{-1}, and (d–f) voltage profiles and cycling performance of Li–O_2 battery with $NiCo_2O_4$/3D-G electrode under 42.5 mA g^{-1} at a limited capacity of 510 mAh g^{-1}.

To clarify the effect of Au/$NiCo_2O_4$/3D-G catalyst on the electrochemical performance of Li–O_2 batteries, XPS and SEM characterizations on the cycled electrodes were performed as displayed in Fig. 7. We can see large particles and small flakes on the electrode after the first discharge to 510 mAh g^{-1} (Fig. 7a). Cross-section view in Fig. 7b reveals that the particles and flakes are only on the top of $NiCo_2O_4$ mushrooms, while the bottom of the mushrooms is intact. The discharged product is confirmed to be Li_2O_2 by selected area electron diffraction (SAED, see Fig. S7b in the ESI†). After the recharge to 510 mAh g^{-1}, the particles disappear completely with the top of the mushroom-like structure exposed again (Fig. 7c). The decomposition of Li_2O_2 is further confirmed by SAED patterns (see Fig. S7c in the ESI†). XPS analysis in Fig. 7d indicates the reversible formation/decomposition of Li_2O_2 upon discharge/charge process, which is further verified by EIS (see Fig. S8 and Table S2 in the ESI†), where the increase/decrease in R_{ct} denotes the reversible deposition/removal of Li_2O_2 on the electrode.

As seen in Fig. 7e,f, Li_2O_2 grows into fluffy, thin-film form on the 10th discharge, which is decomposed after recharge as confirmed by SEM (Fig. 7g) and XPS (Fig. 7h). The morphology

transformation of Li_2O_2 from large particles to thin films is accompanied by gradual decrease in charge potential during cycling, suggesting that thin-film Li_2O_2 is easy to decompose at lower charge potential compared with large Li_2O_2 particles. This can be explained as follows. Large isolated Li_2O_2 particles are insulating and have limited contact with catalysts. Their decomposition requires high charge potential to obtain appreciable charge transport and drive partial delithiation.[31,32] By contrast, thin Li_2O_2 flakes or films have large surface area and distribute homogeneously on the catalyst surface, which benefit the increase in electronic conductivity and promote the charge transfer at Li_2O_2/catalyst interface, thus leading to a lower charge potential.[31,32] It is, therefore, reasonable to infer that Au induces the growth of Li_2O_2 into the fluffy, thin-film form, which in turn, reduces the charge potential. Directing the growth of Li_2O_2 was also observed for other noble metals supported on carbon materials.[24,26,31] In contrast, after the 10th discharge, large particles on the $NiCo_2O_4$/3D-G electrode can be seen (see Fig. S9a in the ESI†). After the subsequent charge, large particles are still remained **(**see Fig. S9b in the ESI†), indicating low catalytic activity of $NiCo_2O_4$/3D-G. This can explain the fast failure of the battery with $NiCo_2O_4$/3D-G catalyst. These results mean that the performance improvement of Li–O_2 batteries can be achieved by optimizing the structure and component of catalysts.

The formation of byproducts, for instance Li_2CO_3, is not detected during the initial cycles (Fig. 7h). However, side reactions, for example electrolyte decomposition, are unavoidable upon repeated cycling,[47,48] which results in the formation and accumulation of Li_2CO_3. The unobvious Li_2CO_3 in the initial cycles is probably due to the small content of Li_2CO_3 that is undetectable. However, as the cycle number increases, the formation and accumulation of Li_2CO_3 will become obvious (see Fig. S10 in the ESI†). Besides, large Li_2O_2 particles will form due to the degraded catalytic activity of the catalyst and the complete decomposition of large Li_2O_2 upon charge will become difficult with cycling (see Fig. S10 in the ESI†). As a result, the electrode will be passivated by the progressively accumulated, insulating Li_2O_2 and Li_2CO_3, leading to capacity fade and eventual failure of the battery.[11,12]

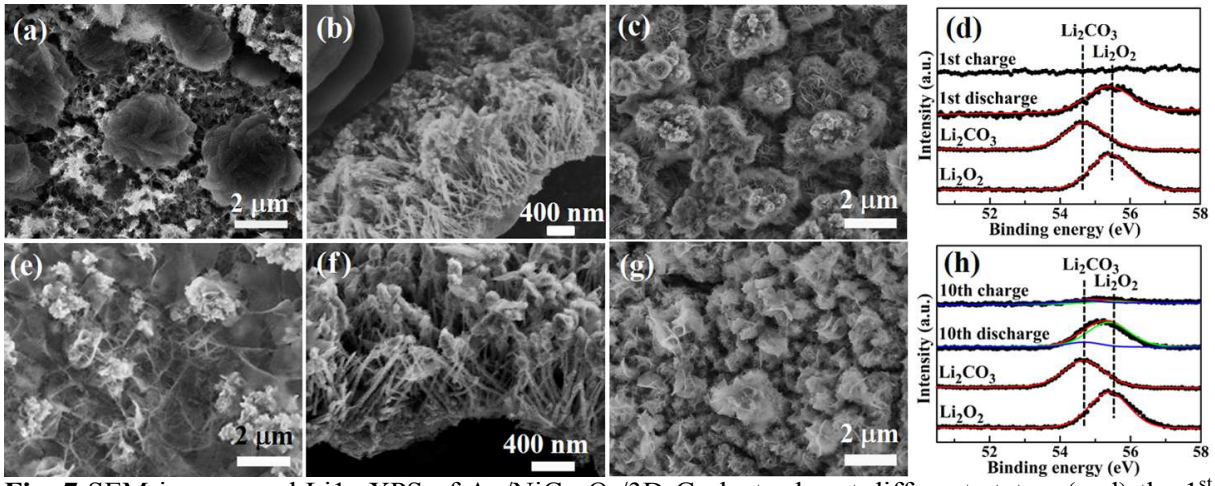

Fig. 7 SEM images and Li1s XPS of Au/$NiCo_2O_4$/3D-G electrodes at different states: (a–d) the 1st cycle and (e–h) the 10th cycle. The batteries are charged and discharged to 510 mAh g^{-1} at 42.5 mA g^{-1}.

Conclusions

In summary, a new design of binder-free catalytic cathode for Li–O_2 batteries has been proposed. The electrode is composed of mushroom-like Au-decorated $NiCo_2O_4$ on 3D-G coated Ni foam. In this design, the intrinsic porous structure of Ni foam ensures barrier-free oxygen transport and electrolyte penetration. Meanwhile, the introduction of Au and graphene can improve the electric conductivity of the electrode. The presence of Au directs the growth of Li_2O_2 dominantly on the top of the mushroom-like $NiCo_2O_4$ that minimizes the contact of Li_2O_2 (or LiO_2) with graphene. Au can guide the growth of Li_2O_2 into thin-flake or thin-film form that facilitates its decomposition at low overpotentials. Therefore, the side reactions related to electrolyte or graphene decomposition can be effectively refrained. Mushroom-like $NiCo_2O_4$ is also indispensable for the good catalytic performance of the Au/$NiCo_2O_4$/3D-G electrode. It provides additional catalytic sites for ORR/OER, and it is good support for both Au particles and Li_2O_2 due to the large surface area with the sheet-like top. In addition, its almost intact wire-like bottom is beneficial for oxygen and Li-ion diffusion. As a result, Li–O_2 batteries with Au/$NiCo_2O_4$/3D-G cathode exhibit good electrochemical properties due to its unique architecture and component.

Acknowledgements

This work was supported by the National Basic Research Program of China (2013CB934001), Key Science and Technology Innovation Team of Zhejiang Province under Grant Number 2010R50013, and Program for Innovative Research Team in University of Ministry of Education of China (IRT13037).

References

1 F. T. Wagner, B. Lakshmanan and M. F. Mathias, *J. Phys. Chem. Lett.*, 2010, **1**, 2204–2219.

2 K. M. Abraham and Z. Jiang, *J. Electrochem. Soc.*, 1996, **143**, 1–5.

3 T. Ogasawara, A. Débart, M. Holzapfel, P. Novák and P. G. Bruce, *J. Am. Chem. Soc.*, 2006, **128**, 1390–1393.

4 G. Girishkumar, B. McCloskey, A. C. Luntz, S. Swanson and W. Wilcke, *J. Phys. Chem. Lett.*, 2010, **1**, 2193–2203.

5. P. G. Bruce, S. A. Freunberger, L. J. Hardwick and J. M. Tarascon, *Nat. Mater.*, 2012, **11**, 19–29.

6 R. Padbury and X. Zhang, *J. Power Sources*, 2011, **196**, 4436–4444.

7 F. J. Li, T. Zhang and H. S. Zhou, *Energy Environ. Sci.*, 2013, **6**, 1125–1141.

8 J. Lu, L. Li, J. B. Park, Y. K. Sun, F. Wu and K. Amine, *Chem. Rev.*, 2014, **114**, 5611−5640.

9 V. Viswanathan, K. S. Thygesen, J. S. Hummelshøj, J. K. Nørskov, G. Girishkumar, B. D. McCloskey and A. C. Luntz, *J. Chem. Phys.*, 2011, **135**, 214704.

10 J. M. Garcia Lastra, J. S. G. Myrdal, R. Christensen, K. S. Thygesen and T. Vegge, *J. Phys. Chem. C*, 2013, **117**, 5568−5577.

11 B. D. McCloskey, A. Speidel, R. Scheffler, D. C. Miller, V. Viswanathan, J. S. Hummelshøj, J. K. Nørskov and A. C. Luntz, *J. Phys. Chem. Lett.*, 2012, **3**, 997−1001.

12 M. M. Ottakam Thotiyl, S. A. Freunberger, Z. Q. Peng and P. G. Bruce, *J. Am. Chem. Soc.*, 2013, **135**, 494−500.

13 R. Black, S. H. Oh, J. H. Lee, T. Yim, B. Adams and L. F. Nazar, *J. Am. Chem. Soc.*, 2012, **134**,

2902−2905.

14 Y. Y. Shao, S. Park, J. Xiao, J. G. Zhang, Y. Wang and J. Liu, *ACS Catal.*, 2012, **2**, 844−857.

15 J. Lu, L. Cheng, K. C. Lau, E. Tyo, X. Y. Luo, J. G. Wen, D. Miller, R. S. Assary, H. H. Wang, P. Redfern, H. M. Wu, J. B. Park, Y. K. Sun, S. Vajda, K. Amine and L. A. Curtiss, *Nat. Commun.*, 2014, **5**, 4895.

16 R. G. Cao, J. S. Lee, M. L. Liu and J. Cho, *Adv. Energy Mater.*, 2012, **2**, 816–829.

17 H. G. Jung, J. Hassoun, J. B. Park, Y. K. Sun and B. Scrosati, *Nat. Chem.*, 2012, **4**, 579–585.

18 H. D. Lim, K. Y. Park, H. Song, E. Y. Jang, H. Gwon, J. Kim, Y. H. Kim, M. D. Lima, R. O. Robles, X. Lepró, R. H. Baughman and K. Kang, *Adv. Mater.*, 2013, **25**, 1348–1352.

19 Y. Cao, Z. K. Wei, J. He, J. Zang, Q. Zhang, M. S. Zheng and Q. F. Dong, *Energy Environ. Sci.*, 2012, **5**, 9765–9768.

20 Y. Cao, M. S. Zheng, S. R. Cai, X. D. Lin, C. Yang, W. Q. Hu and Q. F. Dong, *J. Mater. Chem. A*, 2014, **2**, 18736–18741.

21 Y. M. Cui, Z. Y. Wen and Y. Liu, *Energy Environ. Sci.*, 2011, **4**, 4727–4734.

22 L. X. Zhang, S. L. Zhang, K. J. Zhang, G. J. Xu, X. He, S. M. Dong, Z. H. Liu, C. S. Huang, L. Gu and G. L. Cui, *Chem. Commun.*, 2013, **49**, 3540–3542.

23 Z. Q. Peng, S. A. Freunberger, Y. H. Chen and P. G. Bruce, *Science*, 2012, **337**, 563–566.

24 H. D. Lim, H. Song, H. Gwon, K. Y. Park, J. Kim, Y. Bae, H. Kim, S. K. Jung, T. Kim, Y. H. Kim, X. Lepró, R. Ovalle Robles, R. H. Baughmand and K. Kang, *Energy Environ. Sci.*, 2013, **6**, 3570–3575.

25 C. C. Li, W. Y. Zhang, H. X. Ang, H. Yu, B. Y. Xia, X. Wang, Y. H. Yang, Y. Zhao, H. H. Hng and Q. Y. Yan, *J. Mater. Chem. A*, 2014, **2**, 10676–10681.

26 J. J. Xu, Z. L. Wang, D. Xu, L. L. Zhang and X. B. Zhang, *Nat. Commun.*, 2013, **4**, 2438.

27 D. Oh, J. F. Qi, Y. C. Lu, Y. Zhang, Y. Shao Horn and A. M. Belcher, *Nat. Commun.*, 2013, **4**, 2756.

28 R. Younesi, M. Hahlin, F. Björefors, P. Johansson and K. Edström, *Chem. Mater.*, 2013, **25**,

77–84.

29 F. J. Li, D. M. Tang, Z. L. Jian, D. Q. Liu, D. Golberg, A. Yamada and H. S. Zhou, *Adv. Mater.*, 2014, **26**, 4659–4664.

30 F. J. Li, D. M. Tang, Y. Chen, D. Golberg, H. Kitaura, T. Zhang, A. Yamada and H. S. Zhou, *Nano Lett.*, 2013, **13**, 4702–4707.

31 X. Huang, H. Yu, H. T. Tan, J. X. Zhu, W. Y. Zhang, C. Y. Wang, J. Zhang, Y. X. Wang, Y. B. Lv, Z. Zeng, D. Y. Liu, J. Ding, Q. C. Zhang, M. Srinivasan, P. M. Ajayan, H. H. Hng and Q. Y. Yan, *Adv. Funct. Mater.*, 2014, **24**, 6516–6523.

32 M. D. Radin and D. J. Siegel, *Energy Environ. Sci.*, 2013, **6**, 2370–2379.

33 S. X. Cai, D. S. Zhang, L. Y. Shi, J. Xu, L. Zhang, L. Huang, H. R. Li and J. P. Zhang, *Nanoscale*, 2014, **6**, 7346–7353.

34 H. Wang, D. S. Zhang, T. T. Yan, X. R. Wen, J. P. Zhang, L. Y. Shi and Q. D. Zhong, *J. Mater. Chem. A*, 2013, **1**, 11778–11789.

35 B. G. Choi, S. J. Chang, Y. B. Lee, J. S. Bae, H. J. Kim and Y. S. Huh, *Nanoscale*, 2012, **4**, 5924–5930.

36 B. Sun, X. D. Huang, S. Q. Chen, Y. F. Zhao, J. Q. Zhang, P. Munroe and G. X. Wang, *J. Mater. Chem. A*, 2014, **2**, 12053–12059.

37 X. H. Cao, Y. M. Shi, W. H. Shi, G. Lu, X. Huang, Q. Y. Yan, Q. C. Zhang, H. Zhang, *Small*, 2011, **7**, 3163–3168.

38 J. F. Marco, J. R. Gancedo, M. Gracia, J. L. Gautier and E. Ríos, *J. Solid State Chem.*, 2000, **153**, 74–81.

39 C. Z. Yuan, J. Y. Li, L. R. Hou, L. Yang, L. F. Shen and X. G. Zhang, *J. Mater. Chem.*, 2012, **22**, 16084–16090.

40 T. Choudhury, S. O. Saied, J. L. Sullivan and A. M. Abbot, *J. Phys. D: Appl. Phys.*, 1989, **22**, 1185–1195.

41 A. Miranda, E. Malheiro, E. Skiba, P. Quaresma, P. A. Carvalho, P. Eaton, B. de Castro, J. A.

Shelnutt and E. Pereira, *Nanoscale*, 2010, **2**, 2209–2216.

42 S. Y. Kang, Y. F. Mo, S. P. Ong and G. Ceder, *Chem. Mater.*, 2013, **25**, 3328–3336.

43 Y. C. Lu, B. M. Gallant, D. G. Kwabi, J. R. Harding, R. R. Mitchell, M. S. Whittingham and Y. Shao Horn, *Energy Environ. Sci.*, 2013, **6**, 750–768.

44 D. Y. Zhai, H. H. Wang, J. B. Yang, K. C. Lau, K. X. Li, K. Amine and L. A. Curtiss, *J. Am. Chem. Soc.*, 2013, **135**, 15364–15372.

45 Y. C. Lu, Y and Shao Horn, *J. Phys. Chem. Lett.*, 2013, **4**, 93–99.

46 H. Zheng, D. D. Xiao, X. Li, Y. L. Liu, Y. Wu, J. P. Wang, K. L. Jiang, C. Chen, L. Gu, X. L. Wei, Y. S. Hu, Q. Chen and H. Li, *Nano Lett.*, 2014, **14**, 4245–4249.

47 B. D. McCloskey, D. S. Bethune, R. M. Shelby, G. Girishkumar and A. C. Luntz, *J. Phys. Chem. Lett.*, 2011, **2**, 1161–1166.

48 R. S. Assary, K. C. Lau, K. Amine, Y. K. Sun and L. A. Curtiss, *J. Phys. Chem. C*, 2013, **117**, 8041–8049.

Table of contents entry

Mushroom-like Au/$NiCo_2O_4$/3D-G cathode on Ni foam exhibits superior catalytic effect for Li–O_2 batteries due to Au induced Li_2O_2 growth.